Simultaneous multi-resonant thermally activated delayed fluorescence and room temperature phosphorescence from biluminescent nitrogen-containing indolocarbazoles

Oliver S. Lee[a,b], Aidan P. McKay,[a] David B. Cordes [a], Malte C. Gather[b,c*] and Eli Zysman-Colman[a*]

[a]Organic Semiconductor Centre, EaStCHEM School of Chemistry, University of St Andrews, St Andrews, UK, KY16 9ST

[b]Organic Semiconductor Centre, SUPA School of Physics and Astronomy, University of St Andrews, St Andrews, UK, KY16 9SS.

[c]Humboldt Centre for Nano- and Biophotonics, Department of Chemistry, University of Cologne, Greinstr. 4-6, 50939 Köln, Germany.

Abstract

Organic biluminescence, the simultaneous emission from both the singlet and triplet excited state manifolds, is a rare and incompletely understood emission process. However, biluminescent compounds have wide-reaching applications, such as in sensing, anti-counterfeiting, and optoelectronics, owing to the complex interplay of excited states having distinct spectral profiles and lifetimes. Herein, we describe the biluminescence of a family of polycyclic aromatic heterocycles known as nitrogen-containing indolocarbazoles (**NICz**). As 1 wt% doped films in polymethylmethacrylate (PMMA), these compounds exhibit dual fluorescence/room temperature phosphorescence (RTP) with λ_{PL} in the near-UV (*ca.* 375 nm) and green (*ca*. 500 nm), respectively, and remarkably long phosphorescence lifetimes extending into the multi-second regime. This RTP is shown to persist even at doping concentrations as low as 0.1 wt%. Additionally, two of the emitters exhibit multi-resonant thermally activated delayed fluorescence (MR-TADF)/RTP biluminescence, which, to the best of our knowledge, would be the first examples of such behavior. Finally, we provide insight into the dependence of these competing emission pathways on the temperature and concentration, with supporting wavefunction-based computations.

Introduction

There are many known mechanisms by which a molecule can emit light, classified on the basis of the excited states that are involved in the emission process (Figure **1**). By far the most common for all-organic molecules is fluorescence, the spontaneous emission of light associated with the relaxation

of an excited state of the same multiplicity as the ground state (Figure **1a**).[1] In most organic emitters, which have a closed-shell configuration in the ground state, this occurs from a singlet excited state and typically has a very short (nanosecond) emission lifetime. Additionally, because high-lying excited states rapidly relax down to the lowest excited state of the same multiplicity via internal conversion, fluorescence is generally only observed from the lowest lying singlet excited state, S_1. A second emission mechanism involves radiative decay from an excited state of a different multiplicity to the ground state, typically the lowest-lying triplet excited state (T_1), and is termed phosphorescence (Figure **1b**).[2] Phosphorescence necessitates a spin-flip, termed intersystem crossing, of the relaxing electron from the triplet excited state, where the electrons of the two singly-occupied molecular orbitals (SOMOs) have parallel spin, to the singlet ground state where they antiparallel spin. Because spin must be conserved during an electronic transition, phosphorescence is formally forbidden in a molecule with well-defined spin states, and as such, the rate of phosphorescence in organic molecules, which is inversely proportional to the energy gap between the triplet excited state and the ground state, is several orders of magnitude slower than either fluorescence or nonradiative decay from S_1 or T_1 and thus is typically not observed. For phosphorescence to become more likely, it is necessary for the singlet and triplet excited states to mix, which is most commonly achieved through spin-orbit coupling (SOC). SOC is dependent on the difference of the symmetry of the orbitals involved in the transitions to the singlet and triplet excited states as well as scaling rapidly with atomic number of the atoms involved in these transitions.[1,3,4] It is for these reasons that transition metal complexes containing platinoid metals are so frequently phosphorescent.[2] As the energy gap between S_1 and T_1 (ΔE_{ST}) is significantly smaller than that between S_1 and S_0, and large SOC in these compounds readily facilitates mixing of the excited states of different multiplicity, ISC outcompetes fluorescence, and so only triplet emission is observed. However, because of the relatively large gap between T_1 and S_0 and the required spin-flip, the rate of phosphorescence is slow compared to the typical rate of fluorescence, with a lifetime that typically ranges from microsecond to seconds.[1] Phosphorescence can also occur from organic compounds, where it is known as room temperature phosphorescence (RTP) in the community. As these compounds typically do not contain any heavy atoms, they show much smaller SOC, and so RTP generally has to rely on strongly suppressing non-radiative decay channels.[5–7]

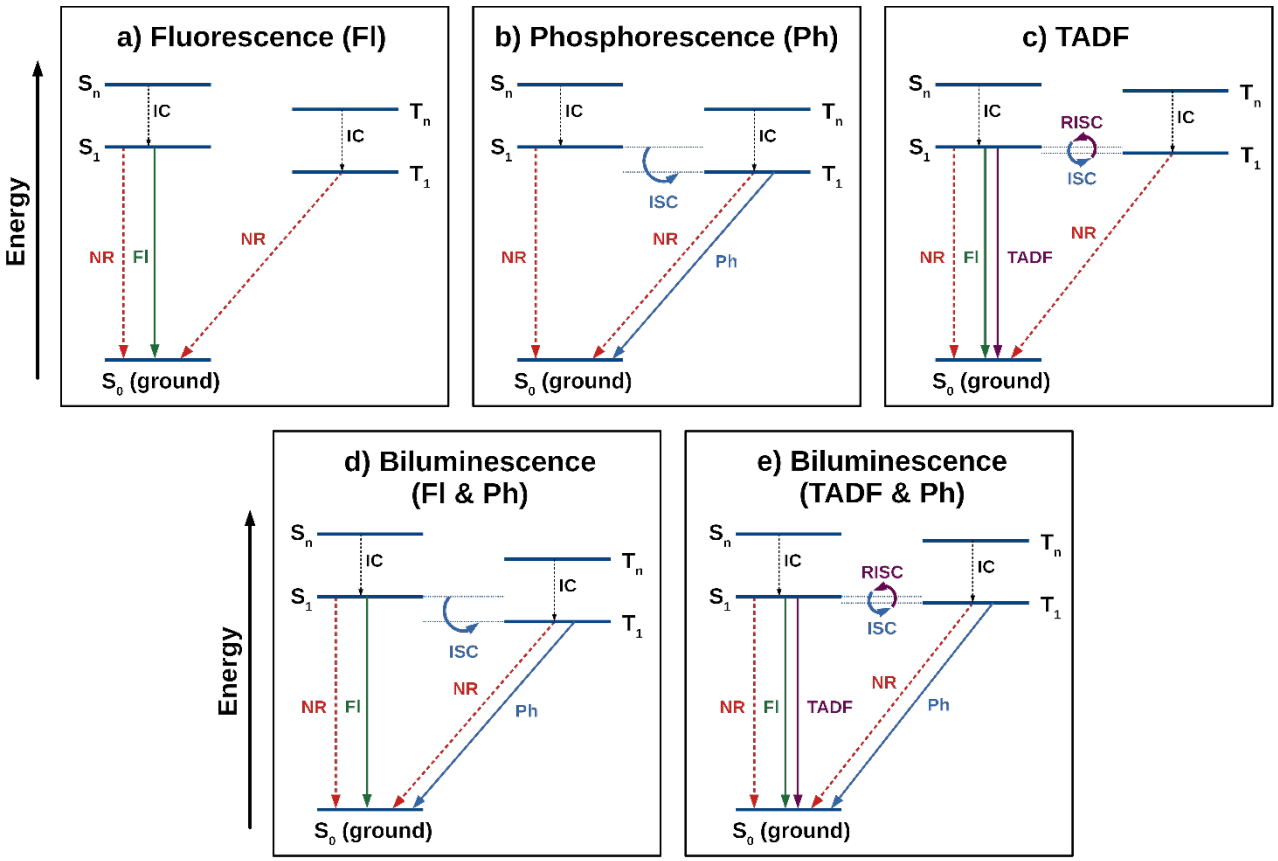

Figure **1**. Simplified Jablonksi diagrams for a) fluorescence, b) phosphorescence, c) thermally activated delayed fluorescence (TADF), d) fluorescence/phosphorescence biluminescence, and e) TADF/phosphorescence biluminescence. IC: internal conversion, NR: non-radiative decay, Fl: fluorescence, Ph: phosphorescence, ISC: intersystem crossing, RISC: reverse-intersystem crossing.

An alternative triplet harvesting mechanism, which does not rely on heavy metals, is thermally activated delayed fluorescence (TADF).[8,9] In this process, the ΔE_{ST} of the emitter is sufficiently small to permit endothermic up-conversion of triplets to singlets *via* reverse-intersystem crossing (RISC). This is possible even with negligible SOC, which also makes phosphorescence a disfavoured radiative decay process.[10] Therefore, TADF materials exhibit dual fluorescence with two distinct lifetimes: 1) prompt fluorescence from radiative decay from directly populated singlet excited states, a process that is identical to the fluorescence introduced above, and therefore has a typical lifetime of nanoseconds; and 2) delayed fluorescence from the same singlet excited state that is repopulated by ISC/RISC cycling.[11] Because this up-conversion relies on a formally forbidden and thermodynamically uphill spin-flip process, it is slow, and thus delayed fluorescence typically occurs on a microsecond-to-millisecond timescale.[1] As RISC is an endothermic process, the rate of TADF is strongly dependent on the temperature, exhibiting faster rates at higher temperatures and slower or absent rates at lower temperature; therefore, this effect manifests itself as an increase in the delayed

emission at higher temperatures. This is opposite to the behaviour observed for phosphorescent compounds wherein at higher temperatures there is a decrease in the delayed emission contribution owing to increased non-radiative deactivation of the T_1 state through molecular vibrations.[5] To enable TADF in an emitter it is necessary to adopt a molecular design that minimizes the exchange integral between the frontier orbitals involved in the radiative transition. There are numerous design strategies used in the literature to achieve this, with multi-resonant thermally activated delayed fluorescence (MR-TADF) having received particular attention in recent years. This mechanism relies on a much shorter charge-transfer distance in the $S_1 \rightarrow S_0$ transition than is found in the more traditional donor-acceptor based long-range charger-transfer TADF compounds, resulting in a significantly narrower emission spectrum in the former compared to the latter.[12] Many of the compounds that exhibit MR-TADF emission are based on a p- and/or n-doped nanographene backbone.[13]

Biluminescence, or dual emission, is the simultaneous emission from multiple excited states of the same molecules.[14] This diverse category of emission processes encompasses many different mechanisms, including S_1/S_2 non-Kasha emission which can be observed in some organic molecules such as porphyrins[15,16] and azulenes,[17] and S_1/T_1 dual fluorescence (or TADF)/phosphorescence that is observed in several Cu(I)-based organometallic emitters.[18] Examples of S_1/T_1 biluminescence in all-organic emitters are rare, and the first report of an organic S_1/T_1 biluminescent emitter to be rigorously characterized was only in 2013 by Reineke and co-workers,[19] although the phenomenon itself is older.[9,20,21] The mechanism(s) of these processes are poorly understood, but in qualitative terms they necessitate a careful balance of the rate constants of fluorescence, intersystem crossing, phosphorescence, and non-radiative decay. Additionally, many of the reported examples of S_1/T_1 biluminescence exhibit TADF in addition to conventional fluorescence,[14,19,22,23] which further necessitates the balancing of the rate of reverse-intersystem crossing with the other photophysical processes. Full design rules by which this can be reliably achieved have not yet been established, but it can be assumed that S_1/T_1 biluminescence requires intermediate values of ΔE_{ST} and SOC, to obtain competitive rates from fluorescence/TADF and RTP while minimizing non-radiative decay. Biluminescence promises to be a hugely important field because it possesses two distinct spectral bands with distinct lifetimes, oxygen dependence and, in the case of TADF/RTP biluminescence, contrasting temperature dependences. This enables a diverse range of applications, including: the simultaneous sensing of temperature and oxygen,[24] data security and counterfeit protection,[25,26] and white-light emitting OLEDs.[22] As such, there is enormous value in both providing insight into this mechanism and in introducing new molecular-scaffolds that exhibit biluminescence. In particular, we note that there are no previous reports of a biluminescent MR-TADF/RTP emitter.

With the initial motivation to develop deep-blue/near-UV MR-TADF emitters, and building on our previous work on diindolocarbazole-based emitters,[27] we chose to investigate the photophysical properties of the nitrogen-containing indolocarbazole (NICz) family of emitters. This family of compounds was previously described by Kader *et al.*,[28] and in solution these compounds have been shown to be near-UV fluorescent emitters. However, their photophysical properties in the film state have, to the best of our knowledge, not previously been explored. Here, we evaluated the photophysical properties of four singly substituted NICz molecules, **4NICz**, **5NICz**, **6NICz**, and **7NICZ**, as well as one-doubly substituted molecule, **6,10NICz** (Figure **2**). We find that three of the emitters exhibit dual fluorescence/RTP emission in doped PMMA films, even at very low doping concentrations, and dual MR-TADF/RTP emission in the emitters **6NICz** and **6,10NICz**, which is likely to be the first example of S_1/T_1 biluminescence from a MR-TADF emitter. The lifetimes associated with both the RTP and TADF are very long, with perceptible afterglow from the phosphorescence extending into the multi-second regime. By varying doping concentrations and temperature, we can influence the relative contributions from fluorescence, TADF, phosphorescence, and non-radiative deactivation. Finally, we provide insight into the change in the emissive pathways of the different isomers based on the changing electronics of the pyridine substitution patterns.

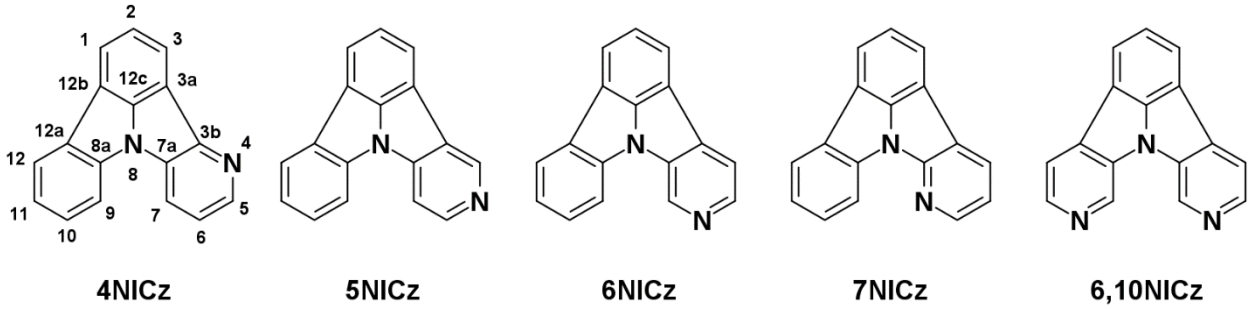

Figure **2**. Structures, names, and numbering scheme of the five emitters investigated.

Computations

We began our investigation by performing a computational analysis of the five emitters. The excited states of multi-resonant TADF molecules emitting *via* a short-range charge-transfer (SRCT) mechanism are well-known to be poorly modelled by time-dependent density functional theory (TD-DFT),[29] owing to the lack of double excitation character in those methods. As such, we opted instead for the second-order algebraic diagrammatic construction method (ADC(2)),[30–32] which we had previously demonstrated to accurately predict the properties of MR-TADF emitters.[29,33] All ADC(2)

calculations were performed using the Turbomole package,[34] using the resolution of the identity approximation (RI) to reduce the calculation duration,[35] spin-component scaling (SCS) for improved accuracy,[36] and the cc-pVDZ basis set.[37–39] Full computational details are available in the Supporting Information (Section S1).

We first optimized the geometry of each emitter (Figure **3**), starting from structures drawn *in silico*. In all cases, the emitters adopt a planar geometry, with a 0.1° or smaller dihedral angle across the central indole nitrogen (**Table 1**), leading to complete conjugation of the π-system throughout each emitter. In general, all five molecules have a low-lying HOMO at around -7.9 eV that is relatively invariant with structure, varying between -7.78 eV for **6NICz** and -7.95 eV for **6,10NICz**. No trend between HOMO energy and pyridine nitrogen position can be ascertained, with the structurally analogous **6NICz** and **6,10NICz** having the highest and lowest HOMO levels, respectively. By contrast, the LUMOs of these compounds are very high lying, with a mean predicted energy of 1.5 eV, and showed greater variation. **6,10NICz** has the most stabilized LUMO (1.17 eV), followed by **6NICz** (1.49 eV), **4NICz** (1.65 eV), **5NICz** (1.68 eV), and **7NICz** (1.73 eV). Here, a structure-property relationship emerges that we will see repeated throughout this study and that can be empirically derived based on the relative position of the pyridine nitrogen to that of the central indole nitrogen. Namely, structures in which the pyridine N is situated in an *ortho*- or *para*-like position (**7NICz** and **5NICz**, respectively) tend to have higher energies (LUMO, $\Delta E_{HOMO\text{-}LUMO}$, S_1 and ΔE_{ST}) than those in a *meta*-like position (**4NICz**, **6NICz**, and **6,10NICz**). Among the *meta*-substituted emitters, **6NICz** and **6,10NICz**, which have a nitrogen at the 6-position, have more stabilised LUMOs than **4NICz**, where the nitrogen is instead at the 4-position. As the HOMO energies are insensitive to structural variation, this pattern is naturally reproduced in the calculated HOMO-LUMO gap ($\Delta E_{HOMO\text{-}LUMO}$). The $\Delta E_{HOMO\text{-}LUMO}$ are very large overall, but the greatest occurs in **5NICz** and **7NICz** (9.61 and 9.56 eV, respectively) and smallest in both **6NICz** and **6,10NICz** (9.27 and 9.13 eV, respectively), while the value for **4NICz** is intermediate at 9.61 eV.

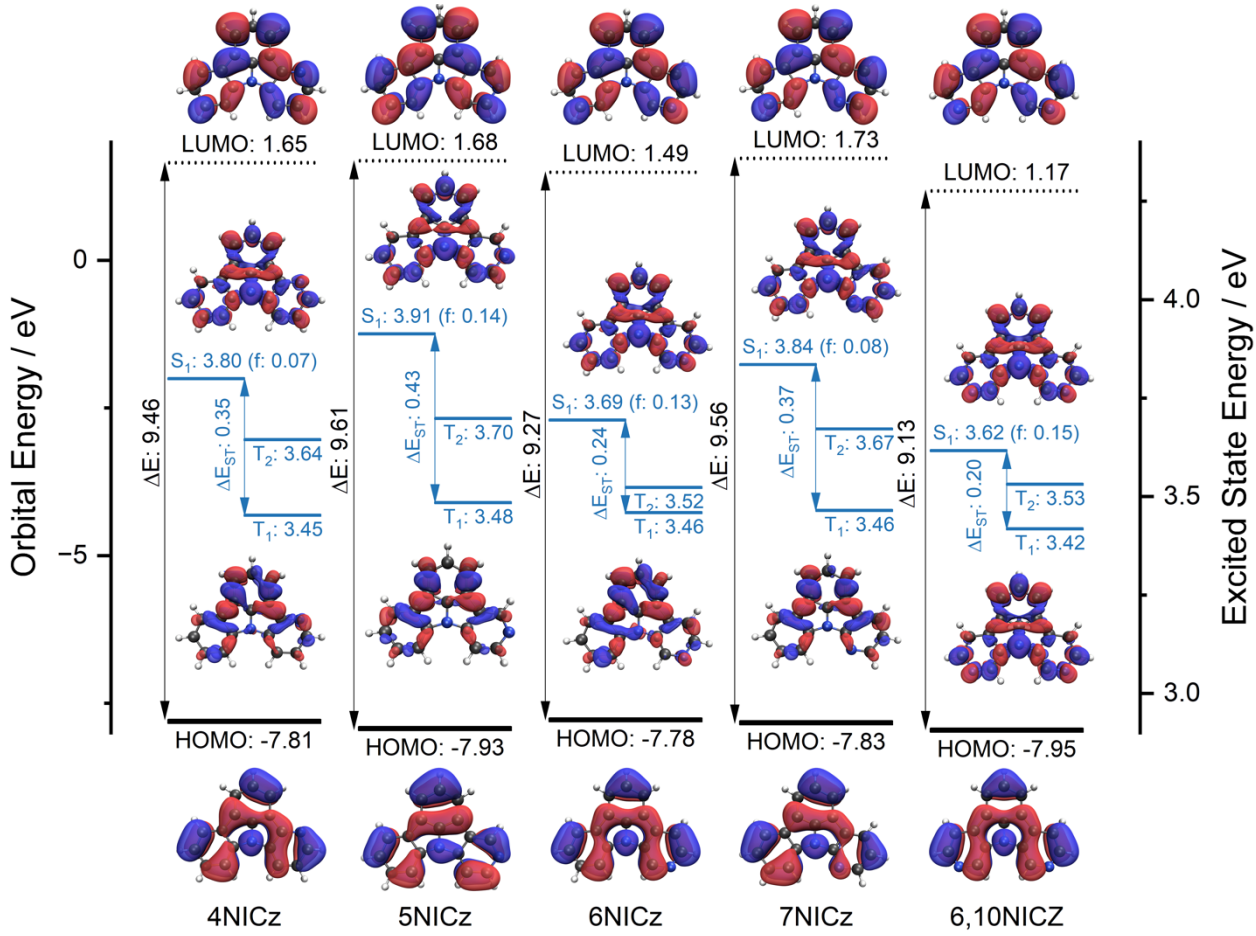

Figure **3**. Computed ground state (HOMO and LUMO) and excited state (S_1,T_1, and T_2) properties of **4NICz**, **5NICz**, **6NICz**, **7NICz**, and **6,10NICz**, calculated at the RI-SCS-ADC(2)/cc-pVDZ level of theory in the gas phase. All values are given in eV. For each emitter, the rendered images are, in order from top to bottom: 1) electron density plot of the LUMO; 2) electron difference density plot between the ground state (S_0) and S_1; 3) electron difference density plot between S_0 and T_1; and electron density plot of the HOMO. All density plots are rendered using an isovalue of 0.02. The red region of the difference density plots corresponds to an increase in electron density in the excited state; the blue to a decrease.

Table **1**. Calculated ground and excited state properties.

Emitter	HOMO / eV	LUMO / eV	$E_{HOMO-LUMO}$ / eV	S_1 / eV	T_1 / eV	ΔE_{ST} / eV	θ / °
4NICz	-7.81	1.65	9.46	3.80	3.45	0.35	< 0.1
5NICz	-7.93	1.68	9.61	3.91	3.48	0.43	< 0.1
6NICz	-7.78	1.49	9.27	3.69	3.46	0.24	< 0.1

7NICz	-7.83	1.73	9.56	3.84	3.46	0.37	< 0.1
6,10NICz	-7.95	1.17	9.13	3.62	3.42	0.20	0.1

[a]Calculated at the ground state. [b] Vertical excited states, calculated at the ground-state geometry. [c]The mean dihedral angle between atoms C_7, C_{7a}, N_8, C_{8a}, and C_{7a}, N_8, C_{8a}, C_9. All calculations were performed using the RI-SCS-ADC(2)/cc-pVDZ level of theory, in the gas phase. See Table **S2** for extended excited state calculation results.

In contrast to the variation of the LUMO energies, the electron density plot of the LUMO is identical in all five emitters (Figure **3**), having significant contribution from all carbon and nitrogen atoms except C_2, C_{12c}, and the central N_8 (see Figure **2** for numbering). The HOMO densities, however, form two distinct groups in their distribution. The HOMOs of **6NICz** and **6,10NICz** are symmetrically distributed in a three-tiered radial pattern around the central N_2, while the HOMOs of **4NICz**, **5NICz** and **7NICz** are perturbed away from this symmetry, forming more distinct lobes and overall possessing more nodal planes. Again, the electron density of **4NICz** lies intermediate of the two patterns. The indole nitrogen has significant density in the HOMO but not the LUMO because of its conjugated lone pair. The peripheral pyridyl nitrogen is noticeably electron-accepting in **6NICz** and **6,10NICz**, having density only in the LUMO, while in **5NICz** and **7NICz** it has both accepting and donating character, reflected in contributions to both frontier molecular orbitals. In general, there is incomplete separation of the HOMO-LUMO densities in all five emitters, which results in both a larger S_1 oscillator strength and ΔE_{ST}.

The calculated S_1 energies are all very high for a conjugated organic compound (Table **1**), mirroring both the magnitude and the trend of the large calculated HOMO-LUMO gaps, with all excited-state energies lying > 3.1 eV. The lowest S_1 energy is 3.62 eV in **6,10NICz** and the highest is 3.91 eV in **5NICz**. The S_0-S_1 oscillator strengths (*f*) do not follow this pattern, however, with values of *ca.* 0.14 for **5NICz**, **6NICz**, and **6,10NICz** while for **4NICz** and **7NICz** the value is half that at *ca.* 0.07. The T_1 energies, on the other hand, vary very little with structure, changing by only 60 meV between **6,10NICz** (3.42 eV) and **5NICz** (3.48 eV). As such, the trend in calculated ΔE_{ST} matches that for the S_1 energies, with **6,10NICz** and **6NICz** having the smallest ΔE_{ST} at 0.20 and 0.24 eV, respectively, followed by **4NICz** at 0.35 eV, and then **7NICz** and **5NICz** at 0.37 and 0.43 eV, respectively. Notably, both **6NICz** and **6,10NICz** have a predicted ΔE_{ST} that is sufficiently small to show TADF.[29] All five emitters additionally have a T_2 state of different orbital type to S_1 (Figure **S33**) that is energetically intermediate to that of S_1 and T_1 (T_2 = 3.64, 3.70, 3.52, 3.67, and 3.53 for **4NICz**, **5NICz**, **6NICz**, **7NICz**, **6,10NICz** respectively). This has been shown to be beneficial for enhancing RISC.[40,41]

By calculating the difference in total electron density between each excited state and the ground state (S_0), it is possible to visualize the spatial distribution of each excited state (Figure **3**). The S_1 density is identical across all five emitters and demonstrates clear SRCT character, i.e. there is an alternating pattern of increasing and decreasing density on the donor and acceptor atoms; this is the behaviour typically observed for MR-TADF compounds. The T_1 density distributions show greater variation than the S_1, despite the consistency in T_1 energies, and form three distinct groups. The *ortho-*/*para-* emitters **5NICz** and **7NICz** possess a largely symmetrical T_1, with a nodal plane passing through C_2, C_{12c} and N_8, while in the *meta*-like emitters **4NICz** and **6NICz** this symmetry is distorted, with additional contribution from C_2 and N_8. Finally, **6,10NICz** uniquely adopts the same distribution in its T_1 state as its S_1 state because the T_1 and T_2 excited states are inverted (Figure **S33**).

Synthesis

4NICz, **5NICz**, **6NICz**, **7NICz**, and **6,10NICz** were synthesized according to the scheme reported by Kader *et al.*,[28] full synthetic details are provided in the supplementary information. The structures of all intermediates and target compounds were unambiguously verified using ^{1}H NMR and ^{13}C NMR spectroscopy. The target compounds **4NICz, 5NICz, 6NICz, 7NICz,** and **6,10NICz** were additionally characterized by HRMS, melting point determination, and single-crystal X-ray diffraction (Figure **S32**). The purity of **4NICz, 5NICz, 6NICz, 7NICz,** and **6,10NICz** was confirmed *via* HPLC (Figures **S11**, **S16**, **S21**, **S26**, and **S31**).

Solution-state Photophysics

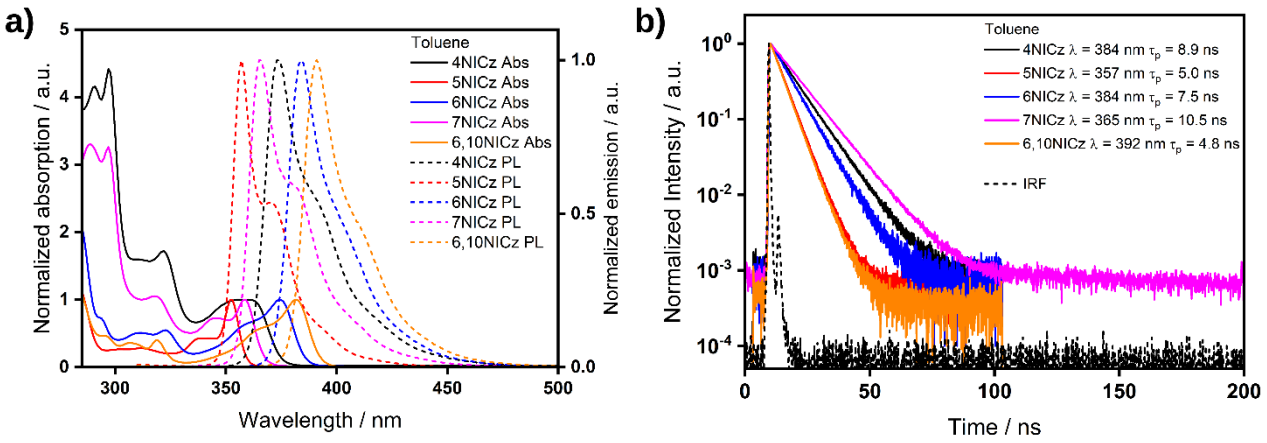

Figure **4**. a) The UV-Vis absorption and photoluminescence (PL) spectra of the emitters in optically dilute toluene solutions (~10^{-5} M), Abs: absorption, PL: photoluminescence. The absorbance has been normalized to the band at *ca.* 350 – 375 nm. λ_{exc} = 297 nm (**4NICz**), 287 nm (**5NICz**), 325 nm (**6NICz**), 297 nm (**7NICz**) and 286 nm (**6,10NICz**). b) Time-resolved PL decays of the emitters

in optically dilute solutions (~10^{-5} M) recorded by time-correlated single photon counting (TCSPC), λ_{exc} = 375 nm. λ values in the legend indicate the emission collection wavelength for each compound; τ_p values represent results of a monoexponential fit to the data. IRF: instrument response function.

There are three distinct features in the UV-Vis absorption spectra of each emitter in dilute toluene solution (Figure **4a**). These are: 1) a low energy band with a peak between 350 – 400 nm with an additional high-energy resolved shoulder; 2) a band with a peak around 320 nm; and 3) a structured high-energy band with a peak below 300 nm. The high-energy shoulder of the low-energy band is blue-shifted by ~ 15 nm relative to the main peak and is less intense in all compounds except in **4NICz**, where the shoulder and peak have almost identical intensity. The trend in the λ_{abs} of the low-energy band matches the trend in the predicted S_1 energies, but the energies are generally more stabilized (Table **2**). The magnitude of the molar attenuation coefficient of the low energy band (ε) is roughly comparable for **4NICz**, **7NICz** and **6,10NICz** (ε = 8.0, 8.2, and 9.5 10^3 M^{-1} cm^{-1}, respectively), while it is approximately double and triple this value for **6NICz** and **5NICz** (ε = 14.0 10^3 M^{-1} cm^{-1}) and (ε = 22.9 10^3 M^{-1} cm^{-1}), respectively. Considering the moderate absorptivity and low energy of this band, we assign it to the SRCT absorption of the ring system (S_1). The absorptivity data reported here in toluene is similar, both in trend and absolute values, to those previously reported by Kader *et al.* in dichloromethane.[28]

Table **2**. Selected photophysical properties in dilute toluene solution.

Emitter	$\lambda_{abs,1}$ / nm (shoulder)	$\varepsilon_{abs,1}$ / $10^3 M^{-1}cm^{-1}$ (shoulder)	λ_{PL} / nm (shoulder)	Stokes Shift / nm (/ eV)	$FWHM_{PL}$ / nm	Φ_{PL}[a] / % (Air)	τ_P[b] / ns
4NICz	360 (353)	8.0 (7.9)	374 (393)	14 (0.13)	27	11 (6)	8.9
5NICz	352 (340)	22.9 (9.7)	357 (371)	5 (0.05)	22	24 (12)	5.0
6NICz	374 (359)	14.0 (8.9)	384 (404)	10 (0.09)	24	53 (50)	7.5
7NICz	359 (345)	8.2 (6.0)	365 (381)	6 (0.06)	26	24 (15)	10.5
6,10NICz	382 (365)	9.5 (5.4)	391 (412)	9 (0.07)	23	15 (12)	4.8

[a]Photoluminescence quantum yield of degassed and aerated solutions. [b]Prompt decay lifetime of emission, λ_{exc} = 375 nm. No delayed lifetimes were detected for any of the emitters. All spectra were obtained in optically dilute solutions (~10^{-5} M). See Table **S3** for full absorption data.

In contrast to the lowest energy band, which shifts with the varying position of the pyridine N, the energy of the medium-energy band is largely invariant. It is most red-shifted in **6NICz** at 323

nm, while it is the most blue-shifted in **5NICz** at 312 nm, a difference of only 11 nm across all five structures. Similar to the profile of the lowest energy band, there is a blue-shifted, lower intensity shoulder of the medium energy band in **4NICz**, **6NICz** and **6,10NICz**, appearing approximately 10 nm shorter in wavelength; however, this shoulder is absent from the spectra of **5NICz** and **7NICz**. The ratio of the intensity between the low-energy and medium-energy bands (Table **S3**) trends very well with the ratio of the calculated oscillator strengths between the transitions to the S_1 and S_2 states (Table **S2**. Specifically, f_{S1} and $\varepsilon_{abs,1}$ are both less intense than f_{S2} and $\varepsilon_{abs,2}$ in **4NICz** and **7NICz**, but f_{S1} and $\varepsilon_{abs,1}$ are more intense than f_{S2} and $\varepsilon_{abs,2}$ in **5NICz**, **6NICz**, and **6,10NICz**. Considering this, and that the calculated S_2 energies are predicted to be invariant with molecular structure, we assign this medium energy-band to a transition to S_2.

The photoluminescence (PL) spectrum of each emitter in toluene shows a single, narrow, high-energy band with a peak, λ_{PL}, < 400 nm (Figure **4**). The trend in the λ_{PL} mirrors that for the lowest-energy absorption band and the calculated S_1 energies, with the highest energy emitter being **5NICz** (357 nm), followed by **7NICz** (365 nm), **4NICz** (374 nm), **6NICz** (384 nm) and **6,10NICz** (391 nm). Each emitter exhibits a remarkably small Stokes shift of < 0.14 eV (< 15 nm, Table **2**), which is consistent with both the short-range charge transfer excited state character and their rigid structure. Having a mirror-image profile to that of the lowest energy absorption band, the PL spectra have a lower intensity, lower energy shoulder, which is typical for vibrational sub-states. Despite the broadening induced by the shoulder, the full width at half-maximum (FWHM) of each emission band is extremely narrow, ranging from 27 nm in **4NICz**, to just 22 nm in **5NICz**. In air, the photoluminescence quantum yield, Φ_{PL}, of the emitters ranges from 50% for **6NICz,** to 15% (**7NICz**) 12% (**5NICz**), 12% (**6,10NICz**), and 6% (**4NICz**). Under deaerated conditions, the Φ_{PL} of **4NICz**, **5NICz** and **7NICz** increase by a factor of 1.8, 2.0, and 1.6 respectively, while the Φ_{PL} of **6NICz** and **6,10NICz** remained relatively constant, changing by only a factor of 1.1 and 1.3, respectively (Table **2**).

Analysis of the time-resolved PL decays reveals the kinetics of the photoluminescence (Figure **4b**). For all emitters, there is a prompt, monoexponential fluorescence decay process, with **6,10NICz** possessing the fastest decay with lifetimes (τ_{PL}) of 4.8 ns, followed by **5NICz** at 5.0 ns, **6NICz** at 7.5 ns, **4NICz** at 8.9 ns, and the slowest being **7NICz** at 10.5 ns **(**Table **2**). There is no discernible pattern between the photoluminescence lifetimes and structure. No delayed emission was detected from any of the emitters, indicating an absence of triplet related processes in this medium.

Polymethylmethacrylate (PMMA) photoluminescence study

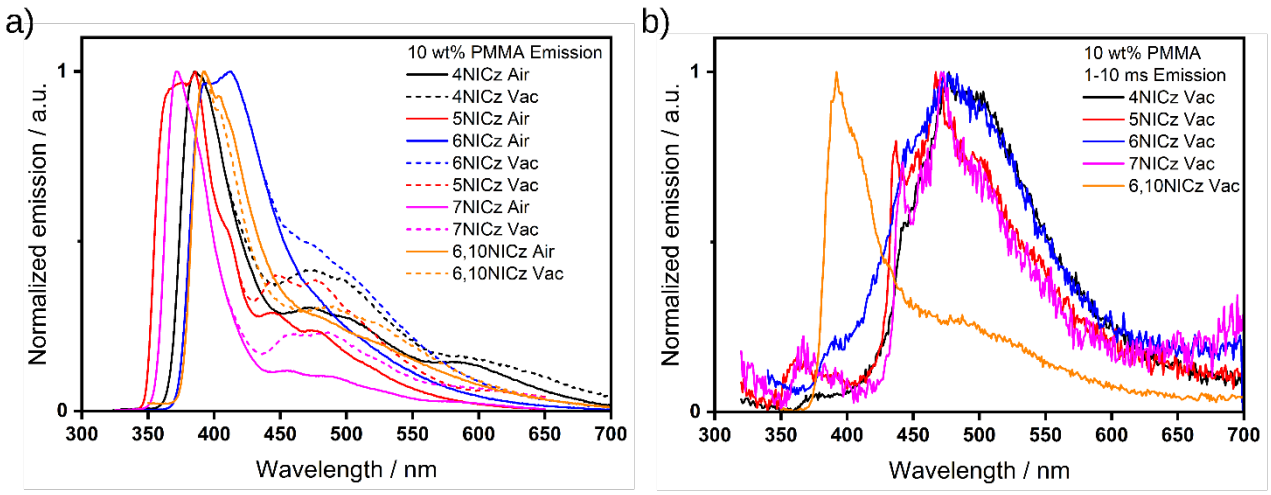

Figure **5**. a) PL spectra of 10 wt% doped films in PMMA in air (solid lines) and under vacuum (dashed lines). The PL under vacuum has been cut at high energy where it matches the PL in air for clarity, i.e. at approximately 400 nm for **4NICz**, **5NICz**, **7NICz** and **6,10NICz**, and 450 nm for **6NICz**. b) Time-gated PL spectra (1-10 ms) under vacuum. λ_{exc} = 295 nm (**4NICz**), 280 nm (**5NICz**), 282 nm (**6NICz**), 294 nm (**7NICz**) and 278 nm (**6,10NICz**) for both a) and b).

We next investigated the photophysical properties of the emitters when dispersed in the inert polymeric host, polymethylmethacrylate (PMMA), first at a doping concentration of 10 wt% emitter compared to the host. When recorded in air, the PL spectrum of each emitter was noticeably broader compared to that in toluene, which is unusual considering the suppression of molecular vibrations that is induced by the solid matrix compared to the free-flowing solution. The degree of broadening experienced by each emitter is not constant, with **6NICz** and **5NICz** having a FWHM that is 3.0× and 2.6× wider than in toluene, respectively, while the FWHM of **6,10NICz** and **4NICz** are approximately twice as wide (1.9× and 1.8×, respectively), and the FWHM of **7NICz** remained relatively narrow, being only 1.5× wider than in toluene. This broadening is likely caused by contributions to the emission from aggregates, considering the relatively high doping concentration and the planar structure of the emitters. Because of this variable broadening, the λ_{PL} of the 10 wt% doped films in PMMA no longer follows the expected pattern of **6/6,10NICz** > **4NICz** > **5/7NICz**, but in general the PL of all the emitters is slightly red-shifted. However, a similar pattern to the trend in λ_{PL} in toluene is observable in terms of the onset of the emission, except that **6NICz** and **6,10NICz** have almost identical onsets. The shoulder feature observed in solution is largely absent in the film PL, with only **5NICz** retaining a significant shoulder in PMMA.

Strikingly, each compound now exhibits a second, less-intense emission band at longer wavelengths (Figure **5a**, solid lines). In **6NICz** and **6,10NICz** this band is partially masked by the tail of the higher energy emission, assigned to emission from S_1, but in **4NICz**, **5NICz** and **7NICz** distinct peaks can be observed at *ca*. 450, 475 and 500 nm, with an additional peak at 590 nm in **4NICz** only. Under vacuum (Figure **5a**, dashed lines), the intensity of this low-energy band increases significantly relative to the intensity of the S_1 band, and clear peaks can now be observed in the steady-state PL spectra of all five emitters. The shape of the S_1 band, meanwhile, is unaffected by the removal of oxygen, except in **6,10NICz**, which is slightly narrower under vacuum. The onset of emission is identical in all cases under both aerated and deaerated conditions.

Time-gated PL spectra acquired between 1 and 10 ms after excitation do not capture the prompt fluorescence, detecting only delayed emission from long-lived excited states (Figure **5b**). Here, a broad emission band is observed with a peak at ~470 nm in **4NICz**, **5NICz**, **6NICz**, and **7NICz** (Table **3**). The time-gated PL spectrum of **6,10NICz**, meanwhile, shows significant delayed emission at the same energy as that observed in the steady-state PL spectrum and which largely masks the emission from any lower-energy PL process; however, a small shoulder can still be observed at ~486 nm. In **4-7NICz**, the peak of the low-energy band varies little with structure, ranging from 467 nm (**5NICz**) to 479 (**6NICz**), and in **5NICz** and **7NICz** it is well resolved into a second peak at higher energy, at 438 and 442 nm, respectively. We assign this low-energy process to room temperature phosphorescence from T_1, for the following reasons: 1) the band is at lower energy than the fluorescence (S_1) band; 2) it is observed as delayed PL; and 3) the λ_{PL} is approximately invariant with structure, matching the trend in T_1 energies predicted by computations. Further evidence for this assignment is provided in emission behaviour of the 1 wt% doped films in PMMA (*vide infra*).

Table 3. Selected photophysical properties in 10 wt% doped films in PMMA.

Emitter	$\lambda_{PL,Fl}$[a] / nm	$\lambda_{PL,Ph}$[b] / nm (shoulder)	$FWHM_{PL}$ / nm (Vac)	$\lambda_{DE,Ph}$[c] / nm (2nd Peak)	Φ_{PL}[e] / % (Vac)	τ_p[f] / ns	τ_d[g] / ms
4NICz	385	472	47 (50)	477	15 (15)	9.8	-
5NICz	386	448 (478)	58 (58)	467 (437)	23 (26)	3.3	-
6NICz	412	475 (505)	72 (86)	479	31 (35)	4.7	-
7NICz	372	483 (457)	38 (38)	472 (442)	23 (25)	10.6	-
6,10NICz	392	485 (523)	44 (52)	~486	10 (12)	3.7	11.9

[a]Peak of the S_1 steady-state band under air. [b]Apparent peak of the steady-state T_1 band under vacuum. [c]Peak of the phosphorescence, as determined by gated emission under vacuum at 1 – 10 ms after excitation. [e]PLQY of the entire PL of the films in air and under vacuum. [f]Prompt decay lifetime of the fluorescence, λ_{exc} = 375 nm. [g]Delayed decay lifetime of the S_1 emission, λ_{exc} = 278 nm. Lifetimes of the phosphorescence were not recorded in this medium, see 1 wt% doped films in PMMA (Table **4**).

In air, the trend found for the Φ_{PL} of the emitters in 10 wt% doped films in PMMA differs slightly from that measured in toluene (Table **3**). The positions of **6,10NICz** and **4NICz** are now reversed, where **6,10NICz** shows the lowest Φ_{PL} (10%), followed by **4NICz** (15%). Meanwhile, **5NICz** and **7NICz** have equivalent Φ_{PL} of 23%, whereas in toluene **7NICz** was slightly brighter, and **6NICz** remains the brightest at 31%. The average Φ_{PL} across all five emitters remains the same as in toluene (20% in PMMA, 19% in toluene), but the spread in Φ_{PL} values is reduced. There is effectively no change in Φ_{PL} under deaerated conditions in 10 wt% doped films in PMMA.

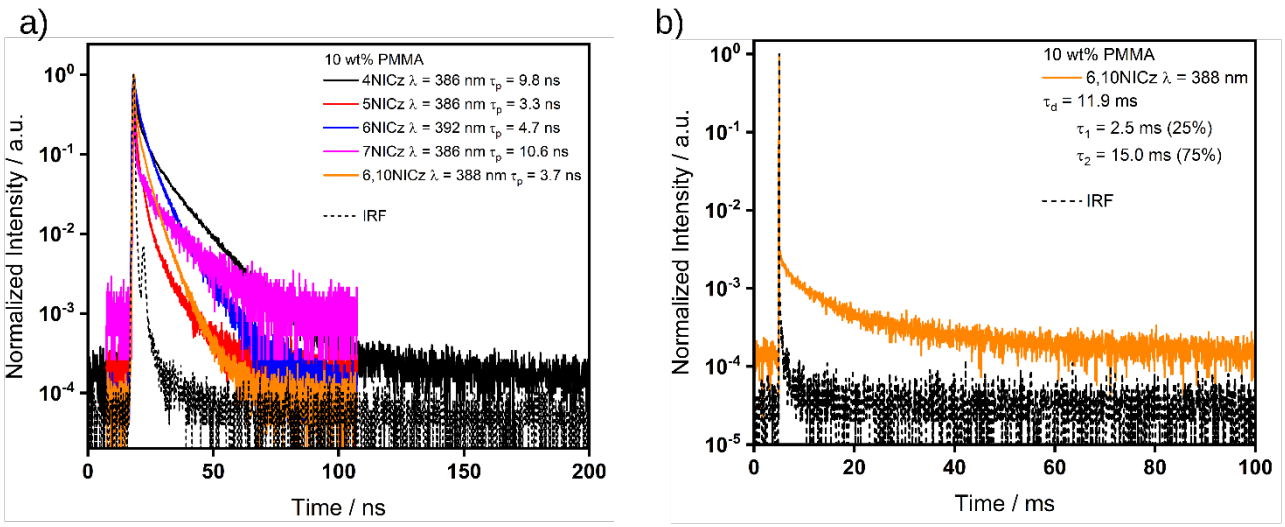

Figure **6**. a) Time-resolved decays of the prompt emission of the emitters in 10 wt% doped films in PMMA, λ_{exc} = 375 nm, collected by TCSPC. b) Time-resolved decays of the delayed emission of **6,10NICz** in 10 wt% doped films in PMMA, collected by multi-channel scaling (MCS), λ_{exc} = 278 nm. The lifetimes given in a) are the average lifetimes of the decay, a breakdown of individual fitting parameters is available in Table **S4**. The lifetimes given in b) are the biexponential fitting parameters of the decay. λ values in the legend indicate the emission collection wavelength for each compound.

Time-resolved PL decay of the prompt emission show biexponential (**4NICz**, **6NICz**, and **7NICz**) or triexponential (**5NICz** and **6,10NICz**) decay kinetics, with average lifetimes that are

comparable to those measured in toluene (Figure **6a**, Table **2** and Table **3**). The trend in the magnitude of the prompt lifetimes of the 10 wt% doped films in PMMA is also the same as that in toluene, except that **5NICz** has a shorter lifetime than **6,10NICz** in the doped PMMA film, while the opposite is true in toluene. Finally, **6,10NICz** exhibits delayed fluorescence, with a lifetime, τ_d, of 11.9 ms, which accounts for the high-energy band observed in the gated PL spectrum (Figure **5b**). We attribute this delayed emission to TADF. Evidence for this assignment is given when we discuss our findings for the 1 wt% PMMA films (*vide infra*), but for now we note that **6,10NICz** exhibits simultaneous TADF/RTP biluminescence at 10 wt% doping in PMMA films. No delayed emission was observed for the other emitters at room temperature.

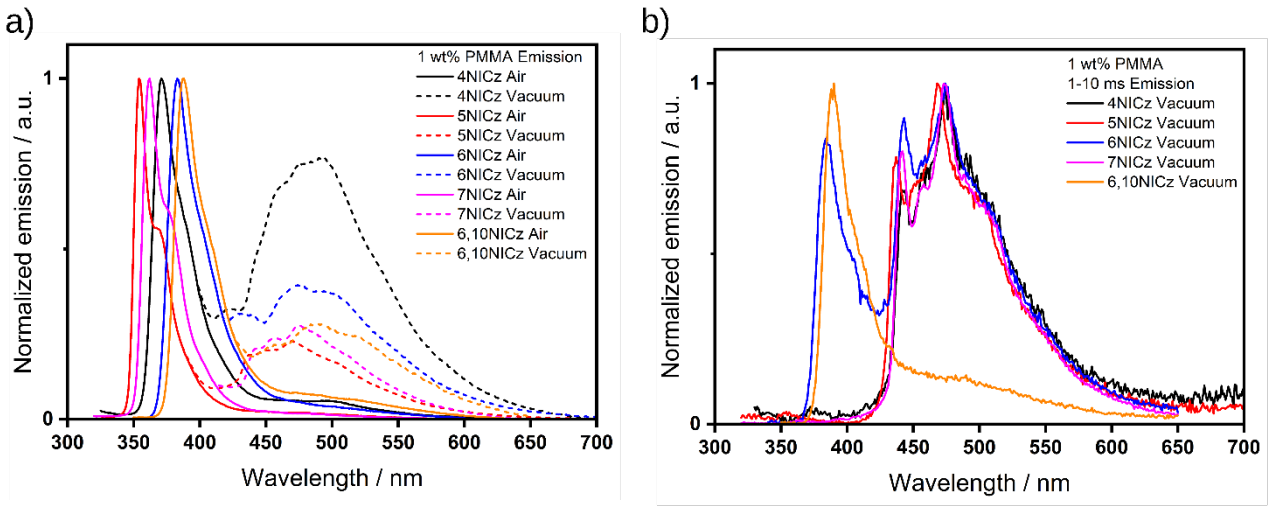

Figure **7**. a) PL spectra of 1 wt% doped films in PMMA in air (solid lines) and under vacuum (dashed lines). For clarity, the PL under vacuum has been cut at high energy where it matches the PL in air, i.e., at approximately 400 nm for **4NICz**, **5NICz**, and **7NICz**, and 425 nm for **6NICz** and **6,10NICz**. b) Time-gated (1-10 ms) PL spectra under vacuum. λ_{exc} = 295 nm (**4NICz**), 280 nm (**5NICz**), 283 nm (**6NICz**), 294 nm (**7NICz**) and 278 nm (**6,10NICz**) for both a) and b).

We next prepared films at 1 wt% emitter doping to mitigate against the formation of aggregates and their potential contribution to the photophysical picture. In air, the steady-state PL spectra were significantly narrowed (Figure **7a**, Table **4**) compared to those of the 10 wt% doped films, with FWHM of 30 nm or less for all five emitters. The PL spectra were also blue-shifted by *ca.* 10 nm, both in terms of the λ_{PL} and the onset, and the expected relationship between the λ_{PL} and molecular structure was re-established. Further, the broad, low-energy emission band at *ca.* 470 nm is absent at this doping concentration in the presence of oxygen. Yet, under vacuum, the low-energy band returns with an equal or greater intensity to that observed in the 10 wt% doped film, relative to the high-energy band (Figure **7a**, dashed line). This highlights the intense oxygen sensitivity of this emission process, which we assign to the same room-temperature phosphorescence from T_1 that we

observed in the 10 wt% doped film. Under vacuum, the time-gated PL spectra (1-10 ms) of **4NICz**, **5NICz**, **6NICz** and **7NICz** exhibit the same broad phosphorescence that was observed in the 10 wt% doped films, but here the band is structured and clearly resolved into two distinct peaks in each of these four emitters. The positions of these peaks are largely invariant with structure, with a minor peak at ~440 nm and a major peak at ~470 nm. For **6,10NICz**, the phosphorescence remains largely hidden by the tail of the delayed fluorescence emission at λ_{PL} of 389 nm, a slight bump is nonetheless observed at *ca.* 485 nm corresponding to emission from T_1. Meanwhile, the time-gated PL spectrum of **6NICz** shows delayed fluorescence at 384 nm that is approximately equal in intensity to the phosphorescence at 473 nm. This behaviour is distinct from the 10 wt% doped films in PMMA, where only delayed emission from T_1 was observed. Therefore, at this lower doping concentration in PMMA, both **6NICz** and **6,10NICz** exhibit dual TADF/RTP emission at room temperature.

Table 4. Selected photophysical properties in 1 wt% doped films in PMMA.

Emitter	$\lambda_{PL,Fl}$[a] / nm (shoulder)	$\lambda_{PL,Ph}$[b] / nm (shoulder)	$FWHM_{PL}$ / nm	$\lambda_{DE,Ph}$[c] / nm (2nd Peak)	τ_p[d] / ns	τ_d[e] / ms	τ_{Ph}[f] / s
4NICz	371	492 (461)	30	474 (443)	-[g]	-[h]	-[i]
5NICz	354 (369)	470 (439)	24	468 (437)	-[g]	-[h]	1.5
6NICz	384	473 (500)	31	474 (443)	3.6	489.2	0.8
7NICz	362 (376)	475 (455)	27	473 (441)	-[g]	-[h]	1.9
6,10NICz	388	487 (521)	30	~485	2.9	34.0	-[j]

[a]Peak of the S_1 steady-state band in air. [b]Apparent peak of the steady-state T_1 band under vacuum. [c]Peak of the phosphorescence, as determined by the time-gated emission (1 – 10 ms), under vacuum. [d]Prompt decay lifetime of the fluorescence. [e]Delayed decay lifetime of the fluorescence. [f]Delayed decay lifetime of the phosphorescence. [g]Not recordable due to the peak position being higher in energy than the excitation source. [h]Not observed. [i]Not recordable in the maximum time window offered by the spectrometer. [j]Not recordable due to the very low intensity.

Unfortunately, the λ_{PL} of each of **4NICz**, **5NICz** and **7NICz** is shorter in wavelength than the pulsed laser excitation source of the fluorimeter, and so reliable decay profiles for the prompt fluorescence could not be obtained for these emitters. However, the lifetimes of the prompt fluorescence of **6NICz** and **6,10NICz** (Figure **8a**) are 1.3× faster than those of the 10 wt% doped films in PMMA, at 3.6 and 2.9 ns, respectively. There is also a delayed fluorescence with τ_d of 489.2 and 34.0 ms for **6NICz** and **6,10NICz**, respectively (Figure **8b**). Compared to the delayed fluorescence observed in the 10 wt% doped films in PMMA, the τ_d of **6,10NICz** is 2.9 times slower in the 1 wt% doped films. The 'switching-on' of TADF at this lower doping concentration in **6NICz** and the simultaneous slowing

of the TADF process in **6,10NICz** highlight the complex interplay of the competing decay processes in these molecules, and the sensitivity of the photophysics to the environment. In the time-gated PL spectra, all five emitters exhibited phosphorescence associated with extremely long lifetimes extending to the time scale of seconds (Figure **8d**). Notably, the phosphorescence of **4NICz** was too long-lived to be accurately fitted over a 10 s time window, but it could be readily observed with the naked eye (Figure **S35**); additionally, the phosphorescence of **6,10NICz** at room temperature was too weak for the decay to be accurately fitted, but the tail of the decay can still be observed in the temperature-dependent TRPL measurement even at room temperature (Figure **9g**). Phosphorescence lifetimes for **4NICz** and **6,10NICz** are thus not reported. The phosphorescence lifetimes, τ_{Ph}, of **5NICz**, **6NICz**, and **7NICz** are 1.5, 0.8, and 1.9 s at room temperature. Finally, a much shorter component to the decay associated with the phosphorescence was recorded over 100/200 ns (Figure **8c**) in all five emitters. We attribute this process to residual prompt fluorescence, considering that the tail of the higher energy emission band clearly extends to overlap with the phosphorescence band (Figure **7a**); we have included the decay and fitted lifetime of this process for completeness. Compared to the prompt fluorescence lifetime, the lifetimes of this "fast" process are 2.7× and 2.0× slower for **6NICz** and **6,10NICz**, respectively, at 9.8 and 4.8 ns.

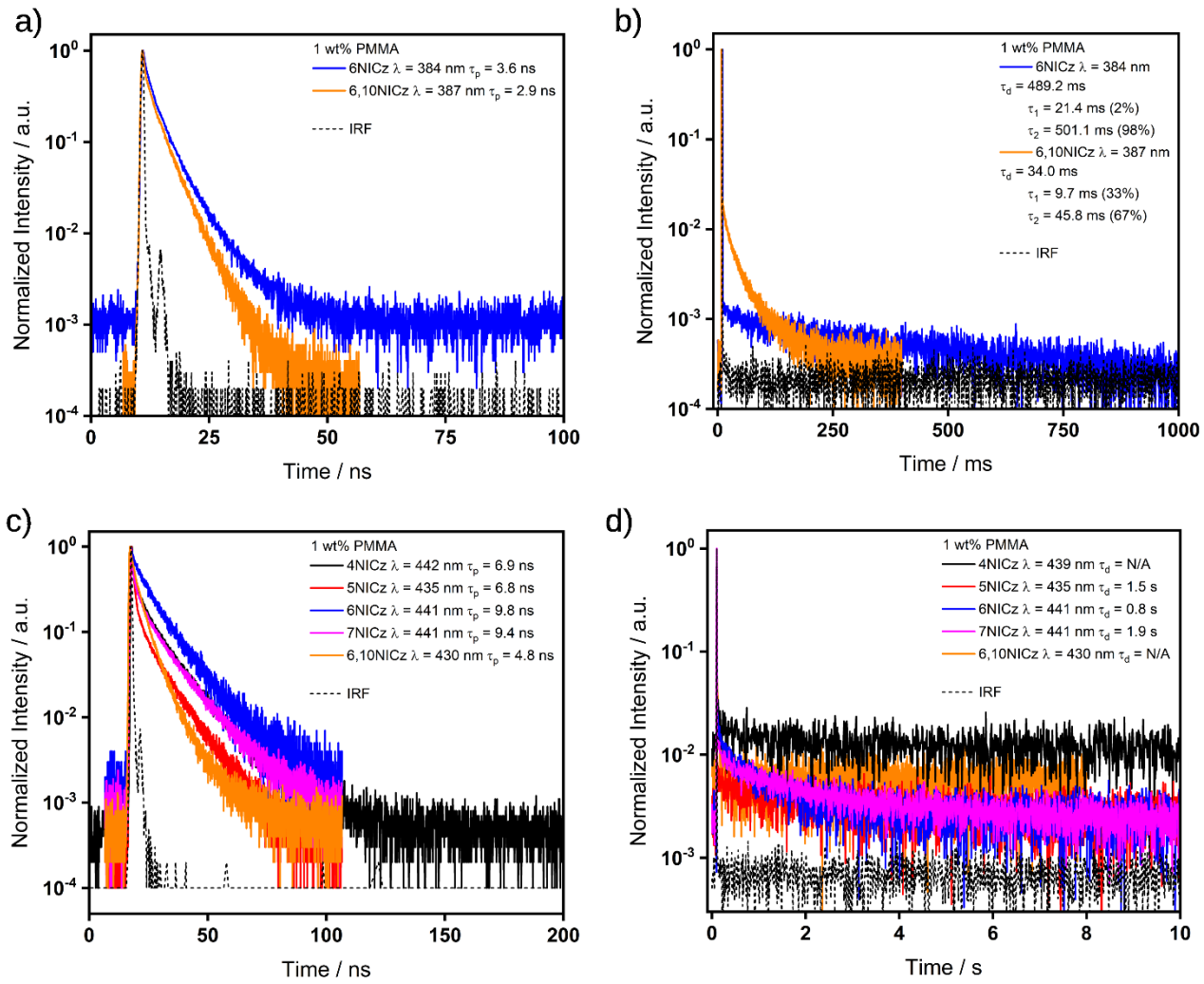

Figure **8**. Time-resolved decays of a) prompt emission (380 – 390 nm), b) delayed emission (380 – 390 nm), c) prompt emission (420 – 450 nm) and d) delayed emission (420 – 450 nm) in 1 wt% doped PMMA films. λ_{exc} = 375 nm (a and c), 283 nm (**4NICz**, b and d), 280 nm (**5NICz**, b and d), 283 nm (**6NICz**, b and d), 294 nm (**7NICz**, b and d), 278 nm (**6,10NICz**, b and d). Decays in a) and c) were collected by TCSPC and b) and d) using the multi-channel scaling (MCS) technique. The lifetimes given are the average lifetimes of the decay, a breakdown of individual fitting parameters is available in Table **S5** and **S6.**

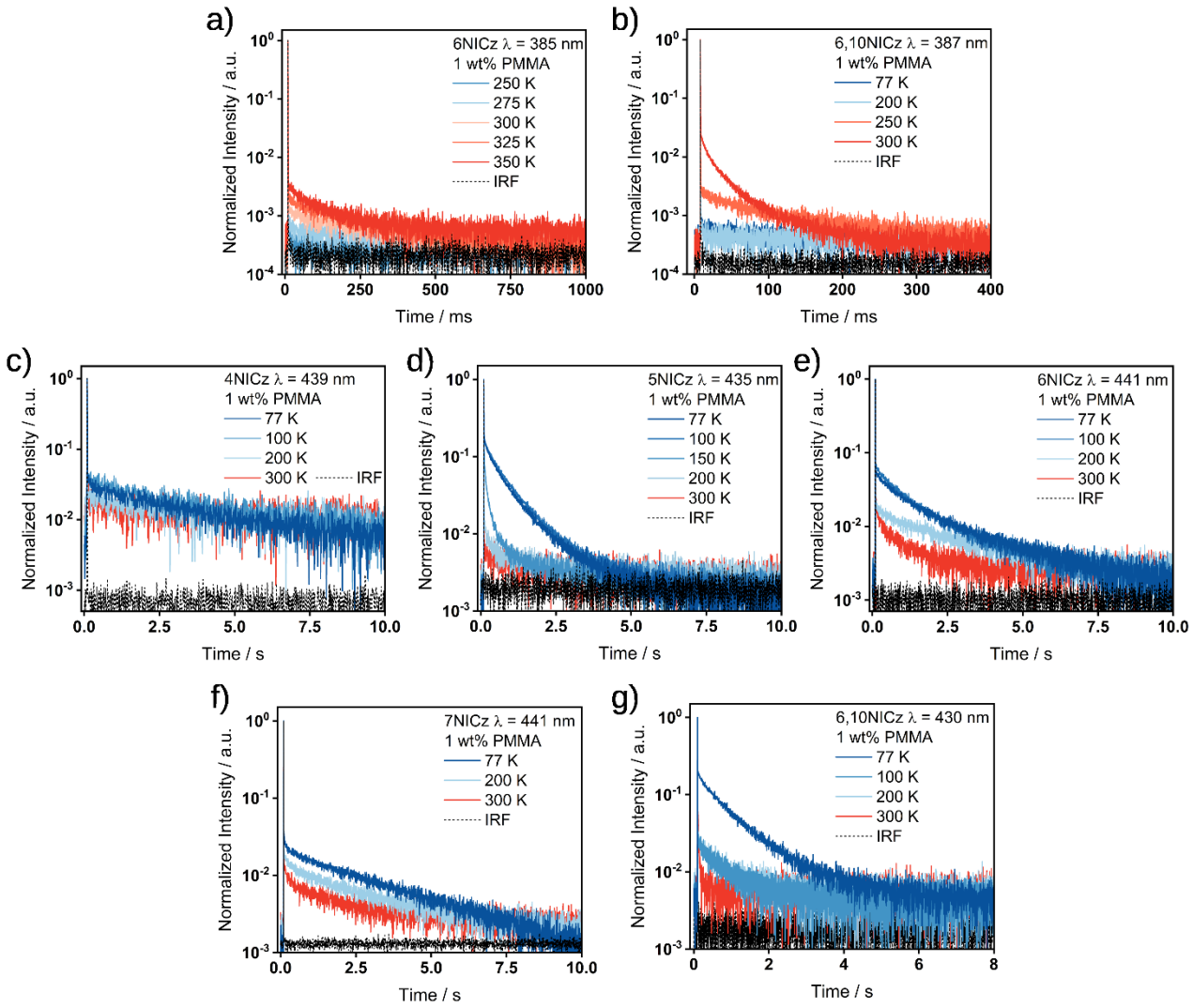

Figure **9**. Temperature-dependant decay processes of the 1 wt% doped PMMA films of a) TADF of **6NICz**, λ_{exc} = 283 nm; b) TADF of **6,10NICz**, λ_{exc} = 278 nm; c) Phosphorescence of **4NICz**, λ_{exc} = 295 nm; d) Phosphorescence of **5NICz**, λ_{exc} = 280 nm; e) Phosphorescence of **6NICz**, λ_{exc} = 283 nm; f) Phosphorescence of **7NICz**, λ_{exc} = 294 nm; g) Phosphorescence of **6,10NICz**, λ_{exc} = 278 nm. All decays were recorded using the multi-channel scaling (MCS) technique.

To fully assign the origin of the delayed emission, we next recorded the change in delayed lifetimes with temperature. The delayed fluorescence observed in **6NICz** and **6,10NICz** is noticeably faster at elevated temperatures (Figure **9a** and **b**), and is assigned as TADF. As all five emitters exhibit negligible solvatochromism (Figure **S34**), this process can be assigned as SRCT emission, which is characteristic of MR-TADF. The ΔE_{ST} of **6NICz** and **6,10NICz** in 1 wt% doped films in PMMA, measured from the difference in the onset of the steady-state PL and time-gated emission (1-10 ms) at 77 K (Figure **S36**, is 0.46 and 0.36 eV, respectively, which explains the very long delayed fluorescence lifetimes observed in this medium. The ΔE_{ST} of **4NICz**, **5NICz** and **7NICz** is 0.59, 0.59

and 0.65 eV, respectively, which are too large for efficient TADF. We note that the ΔE_{ST} of **5NICz** is likely to be slightly underestimated, due to the broadening of the phosphorescence spectrum at low temperature, which makes measuring the true onset difficult. Despite this, the trend in ΔE_{ST} largely matches that predicted by computations, with **6NICz** and **6,10NICz** having the smallest ΔE_{ST}, followed by **4NICz** and **5NICz** and then **7NICz** having the largest ΔE_{ST}.

Meanwhile, the intensity of the low energy phosphorescence in all five emitters shows a characteristic inverse temperature dependence (Figure **9c**, **d**, **e**, **f**, and **g)**. To confirm that the room-temperature phosphorescence originates from the T_1 state, we additionally recorded the change in the time-gated PL spectra with temperature (Figure **10**). For **4NICz** and **7NICz**, the phosphorescence spectra do not change between 77 and 300 K, while for **5NICz** the λ_{Ph} remains the same, but the PL spectra are broadened at lower temperatures. In **6NICz** and **6,10NICz**, the shape of the phosphorescence at 300 K is partially masked by the contribution from the higher energy TADF, but the bump originating from RTP clearly matches the peak position of the phosphorescence at 77 K. The time-gated PL spectra of **6NICz** in particular showcase the competition between TADF and phosphorescence, with the intensity of the TADF decreasing and the intensity of the phosphorescence increasing with decreasing temperature (Figure **10c**). In all cases, the phosphorescence at 77 K matches that observed at room temperature, and so the phosphorescence can be assigned to the radiative decay from the T_1 state.

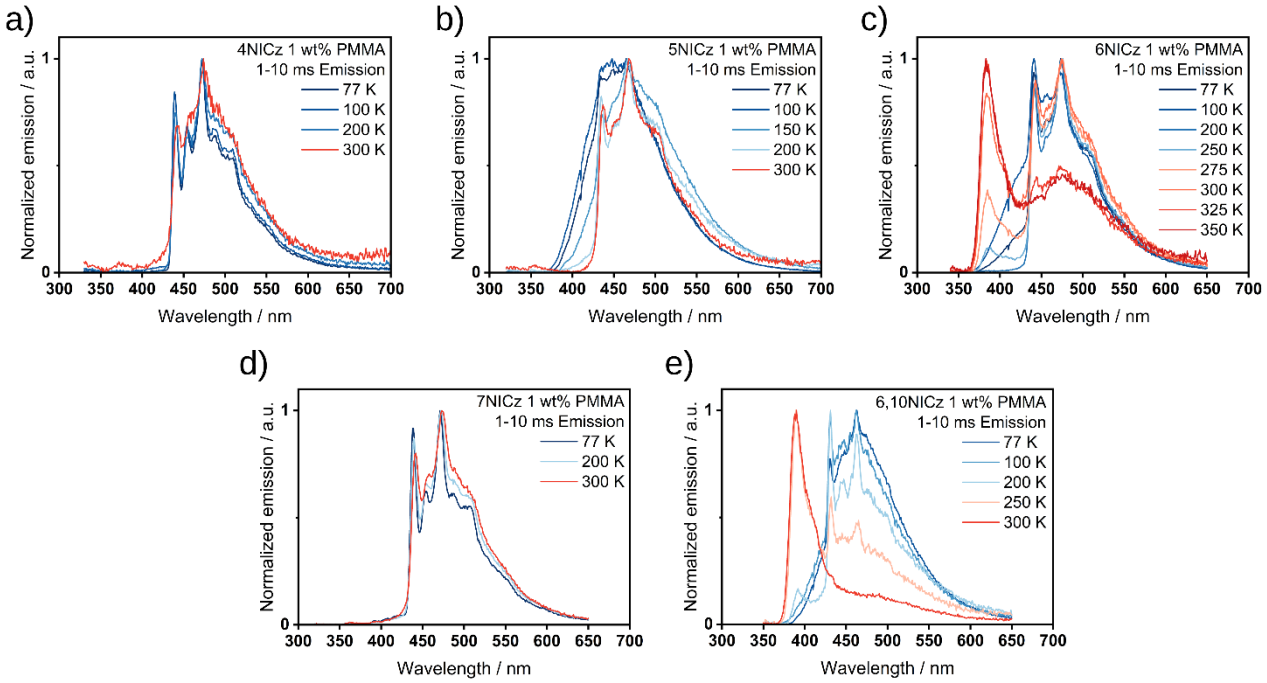

Figure **10**. The change in the time-gated PL spectra (1-10 ms) of a) **4NICz**, b) **5NICz**, c) **6NICz**, d) **7NICz**, and e) **6,10NICz** in 1 wt% doped PMMA films as a function of temperature under

vacuum. λ_{exc} = 295 nm (**4NICz**), 280 nm (**5NICz**), 283 nm (**6NICz**), 294 nm (**7NICz**) and 278 nm (**6,10NICz**).

To ensure that there is no possibility that emission from aggregates contributes to the observed photophysics, we next prepared 0.1 wt% doped films in PMMA. The PL spectra both in air and under vacuum are comparable to the 1 wt% doped film spectra (Figure **11**, black and red lines), with the primary difference being the ratio of the fluorescence to phosphorescence under vacuum. In **4NICz**, **5NICz**, **6NICz**, and **6,10NICz**, there is a decrease in the proportion of phosphorescence to fluorescence in the 0.1 wt% doped films compared to the 1 wt% doped films, but in **7NICz** this is reversed, with a slight increase in the phosphorescence relative to fluorescence in the 0.1 wt% doped films. The time-gated PL also corresponds well to the 1 wt% doped films in PMMA (Figure **S37**), and so the same biluminescence behaviour is preserved at 0.1 wt% emitter concentration. Exceptionally, **5NICz** uniquely has residual fluorescence in the time-gated PL only at 0.1 wt%. However, the brightness of this film was very low and there is significant background scattering from the emission source present in the spectrum, so it is difficult to ascertain the true intensity and nature of this 'delayed' fluorescence. The strong sensitivity of the phosphorescence to the presence of oxygen is conserved in the 0.1 wt% doped films; for example, **6,10NICz** shows no phosphorescence in air (Figure **11e**). Upon increasing the doping concentration to 10 wt%, there is a red-shift in the PL (*vide supra*), and the relative intensity of the fluorescence and phosphorescence continues to change (Figure **11**, blue line). The PL of **5NICz**, **6NICz**, and **6,10NICz** exhibit the greatest proportion of phosphorescence to fluorescence at 10 wt%, while **4NICz** and **7NICz** exhibit the least, highlighting the non-linear dependence of the RTP on doping concentration. For completeness, we have also recorded the steady-state and time-gated PL of the neat films (Figure **S38**, which show distinct emission behaviour from the doped films in PMMA.

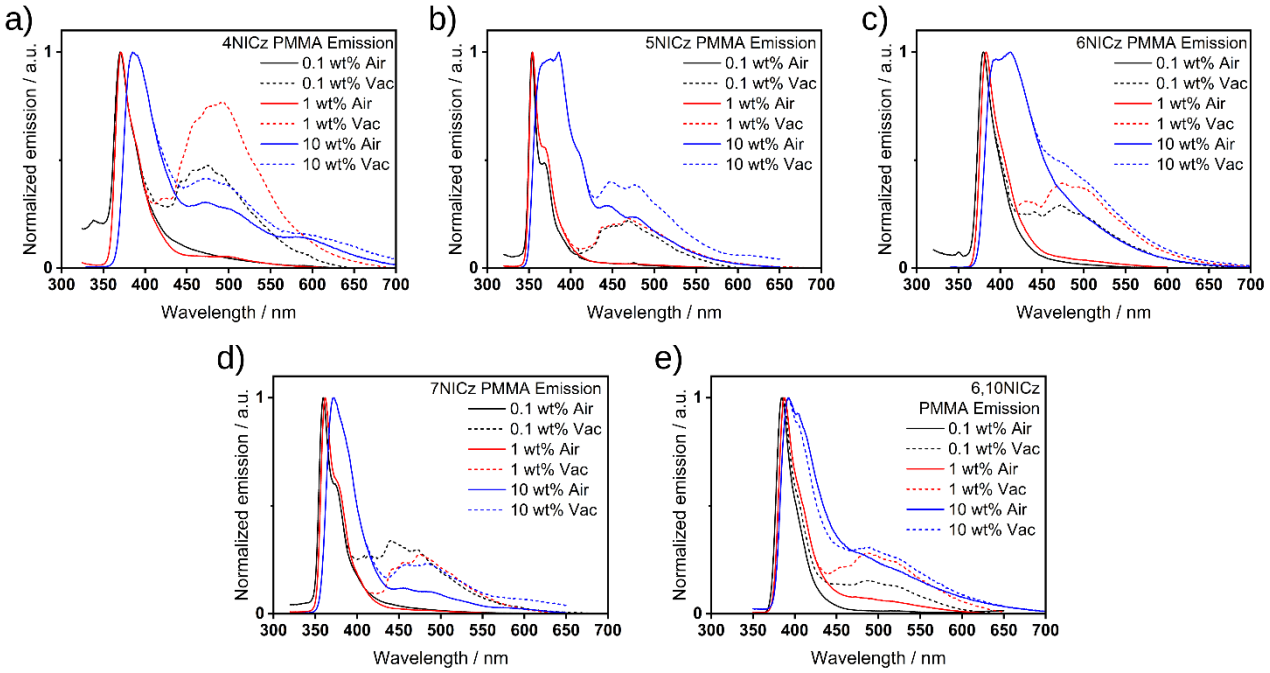

Figure **11**. The change in the PL spectra of a) 4NICz, b) 5NICz, c) 6NICz, d) 7NICz, and e) 6,10NICz in doped PMMA films for different emitter concentrations. λ_{exc} = 295 nm (**4NICz**), 280 nm (**5NICz**), 283 nm (**6NICz**), 294 nm (**7NICz**) and 278 nm (**6,10NICz**). The change in gated PL is shown in Figure **S37**.

We summarize the photophysics of the doped films in PMMA as follows: At 10 wt%, the PL is broadened, red-shifted, and less well resolved compared to lower doping concentrations or solution measurements in toluene due to the influence of intermolecular emission from aggregates. All five of the emitters are biluminescent, with simultaneous emission from the S_1 and T_1 excited states, in the form of fluorescence/phosphorescence for the singly substituted emitters (**4NICz**, **5NICz**, **6NICz**, and **7NICz**) and MR-TADF/phosphorescence for **6,10NICz**. The PL spectra at 1 wt% and 0.1 wt% are equivalent and results from emission from monomolecular species, resulting in narrower, blue-shifted and better resolved spectra. The biluminescence behaviour is preserved in the 10 wt% doped films except that MR-TADF has been switched on in **6NICz** in addition to **6,10NICz**. Finally, the proportion of RTP (relative to fluorescence) shows non-linear dependence on the doping concentration, while the oxygen sensitivity of the RTP is greatest at 1 wt%, of the concentrations tested here.

Conclusions

We have carried out an extensive photophysical survey of five nitrogen-containing indolocarbazoles, supported by a theoretical study using the post-HF SCS-RI-ADC(2) method. In dilute toluene

solution, the five compounds are UV fluorescent emitters with very narrowband emission. The differences in the energy of emission between the five compounds is driven by changes in LUMO level as the position and number of pyridine N substitution changes, while the HOMO level remains largely insensitive to these structural changes. The greatest stabilisation of the LUMO, and therefore the lowest energy of emission, is seen in **6,10NICz**, followed by **6NICz**, **4NICz**, **5NICz** and finally **7NICz**. PMMA films doped with 0.1, 1 and 10 wt% of the different emitters show biluminescence at room temperature, with distinct fluorescence and phosphorescence bands. Additionally, the two *meta*-substituted emitters **6NICz** and **6,10NICz** show multi-resonant thermally activated delayed fluorescence at 1 wt% doping, with **6,10NICz** also exhibiting MR-TADF at 10 wt%. This is, to the best of our knowledge, the first unequivocal demonstration of MR-TADF/RTP type biluminescence in an organic emitter. The RTP persists even at very low-doping concentrations and so is monomolecular in nature. We note that the discovery of MR-TADF/RTP biluminescence in this family of emitters suggests a number of exciting applications for future research, including the sensing of oxygen and/or temperature, and broad-spectrum emission.

Acknowledgements

We thank the Quantum-Materials Centre for Doctoral Training at the University of St Andrews for funding. We acknowledge the Engineering and Physical Sciences Research Council of the UK for support through grants EP/P010482/1 and EP/W007517/1). E.Z.-C. and M.C.G. acknowledge the European Union's Horizon 2020 research and innovation programme under the Marie Skłodowska Curie grant agreement No. 101073045 (TADFsolutions) and the EPSRC (EP/X026175/1) for funding. M.C.G. acknowledges funding from the European Research Council under the European Union's Horizon Europe Framework Programme/ERC Advanced Grant agreement No. 101097878 (HyAngle).

Supporting Information

Melting point analysis, ^{1}H NMR and ^{13}C NMR spectra, HRMS and reverse phase HPLC; supplementary computational data and coordinates; Crystallographic data (CIF). Additional photophysical data. Complete synthetic and photophysical methodology.

References

(1) Wong, M. Y.; Zysman-Colman, E. Purely Organic Thermally Activated Delayed Fluorescence Materials for Organic Light-Emitting Diodes. *Adv. Mater.* **2017**, *29* (22), 1605444. https://doi.org/10.1002/adma.201605444.

(2) Minaev, B.; Baryshnikov, G.; Agren, H. Principles of Phosphorescent Organic Light Emitting Devices. *Phys. Chem. Chem. Phys.* **2014**, *16* (5), 1719–1758. https://doi.org/10.1039/c3cp53806k.

(3) El-Sayed, M. A. Triplet State. Its Radiative and Nonradiative Properties. *Acc. Chem. Res.* **1968**, *1* (1), 8–16. https://doi.org/10.1021/ar50001a002.

(4) El-Sayed, M. A. Spin—Orbit Coupling and the Radiationless Processes in Nitrogen Heterocyclics. *J. Chem. Phys.* **1963**, *38* (12), 2834–2838. https://doi.org/10.1063/1.1733610.

(5) Ma, H.; Lv, A.; Fu, L.; Wang, S.; An, Z.; Shi, H.; Huang, W. Room-Temperature Phosphorescence in Metal-Free Organic Materials. *Ann. Phys.* **2019**, *531* (7), 1800482. https://doi.org/10.1002/andp.201800482.

(6) Hirata, S. Recent Advances in Materials with Room-Temperature Phosphorescence: Photophysics for Triplet Exciton Stabilization. *Adv. Opt. Mater.* **2017**, *5* (17), 1700116. https://doi.org/10.1002/adom.201700116.

(7) Zhao, W.; He, Z.; Tang, B. Z. Room-Temperature Phosphorescence from Organic Aggregates. *Nat. Rev. Mater.* **2020**, *5* (12), 869–885. https://doi.org/10.1038/s41578-020-0223-z.

(8) Endo, A.; Ogasawara, M.; Takahashi, A.; Yokoyama, D.; Kato, Y.; Adachi, C. Thermally Activated Delayed Fluorescence from Sn4+-Porphyrin Complexes and Their Application to Organic Light Emitting Diodes - A Novel Mechanism for Electroluminescence. *Adv. Mater.* **2009**, *21* (47), 4802–4806. https://doi.org/10.1002/adma.200900983.

(9) Delorme, R.; Perrin, F. Durées de Fluorescence Des Sels d'uranyle Solides et de Leurs Solutions,. *J. Phys. Radium* **1929**, *10* (5), 177–186. https://doi.org/10.1051/jphysrad:01929001005017700.

(10) Kaji, H.; Suzuki, H.; Fukushima, T.; Shizu, K.; Suzuki, K.; Kubo, S.; Komino, T.; Oiwa, H.; Suzuki, F.; Wakamiya, A.; Murata, Y.; Adachi, C. Purely Organic Electroluminescent Material Realizing 100% Conversion from Electricity to Light. *Nat. Commun.* **2015**, *6* (May), 8476. https://doi.org/10.1038/ncomms9476.

(11) Tsuchiya, Y.; Diesing, S.; Bencheikh, F.; Wada, Y.; Dos Santos, P. L.; Kaji, H.; Zysman-Colman, E.; Samuel, I. D. W.; Adachi, C. Exact Solution of Kinetic Analysis for Thermally Activated Delayed Fluorescence Materials. *J. Phys. Chem. A* **2021**, *125* (36), 8074–8089. https://doi.org/10.1021/acs.jpca.1c04056.

(12) Madayanad Suresh, S.; Hall, D.; Beljonne, D.; Olivier, Y.; Zysman-Colman, E. Multiresonant Thermally Activated Delayed Fluorescence Emitters Based on Heteroatom-Doped Nanographenes: Recent Advances and Prospects for Organic Light-Emitting Diodes. *Adv. Funct. Mater.* **2020**, *30* (33), 1908677. https://doi.org/10.1002/adfm.201908677.

(13) Hatakeyama, T.; Shiren, K.; Nakajima, K.; Nomura, S.; Nakatsuka, S.; Kinoshita, K.; Ni, J.; Ono, Y.; Ikuta, T. Ultrapure Blue Thermally Activated Delayed Fluorescence Molecules: Efficient HOMO-LUMO Separation by the Multiple Resonance Effect. *Adv. Mater.* **2016**, *28* (14), 2777–2781. https://doi.org/10.1002/adma.201505491.

(14) Behera, S. K.; Park, S. Y.; Gierschner, J. Dual Emission: Classes, Mechanisms, and Conditions. *Angew. Chem. Int. Ed.* **2021**, *60* (42), 22624–22638. https://doi.org/10.1002/anie.202009789.

(15) Terenin, A.; Kobyshev, G.; Lialin, G. ANOMALOUS EMISSION OF CHLOROPHYLL, STIMULATED BY RUBY LASER. *Photochem. Photobiol.* **1966**, *5* (8), 689–691. https://doi.org/10.1111/j.1751-1097.1966.tb05815.x.

(16) Bajema, L.; Gouterman, M.; Rose, C. B. Porphyrins XXIII: Fluorescence of the Second Excited Singlet and Quasiline Structure of Zinc Tetrabenzporphin. *J. Mol. Spectrosc.* **1971**, *39* (3), 421–431. https://doi.org/10.1016/0022-2852(71)90213-X.

(17) Beer, M.; Longuet-Higgins, H. C. Anomalous Light Emission of Azulene. *J. Chem. Phys.* **1955**, *23* (8), 1390–1391. https://doi.org/10.1063/1.1742314.
(18) Hofbeck, T.; Monkowius, U.; Yersin, H. Highly Efficient Luminescence of Cu(I) Compounds: Thermally Activated Delayed Fluorescence Combined with Short-Lived Phosphorescence. *J. Am. Chem. Soc.* **2015**, *137* (1), 399–404. https://doi.org/10.1021/ja5109672.
(19) Reineke, S.; Seidler, N.; Yost, S. R.; Prins, F.; Tisdale, W. A.; Baldo, M. A. Highly Efficient, Dual State Emission from an Organic Semiconductor. *Appl. Phys. Lett.* **2013**, *103* (9), 093302. https://doi.org/10.1063/1.4819444.
(20) Endo, A.; Sato, K.; Yoshimura, K.; Kai, T.; Kawada, A.; Miyazaki, H.; Adachi, C. Efficient Up-Conversion of Triplet Excitons into a Singlet State and Its Application for Organic Light Emitting Diodes. *Appl. Phys. Lett.* **2011**, *98* (8), 2009–2012. https://doi.org/10.1063/1.3558906.
(21) Lewis, G. N.; Lipkin, D.; Magel, T. T. Reversible Photochemical Processes in Rigid Media. A Study of the Phosphorescent State. *J. Am. Chem. Soc.* **1941**, *63* (11), 3005–3018. https://doi.org/10.1021/ja01856a043.
(22) Bhattacharjee, I.; Acharya, N.; Bhatia, H.; Ray, D. Dual Emission through Thermally Activated Delayed Fluorescence and Room-Temperature Phosphorescence, and Their Thermal Enhancement via Solid-State Structural Change in a Carbazole-Quinoline Conjugate. *J. Phys. Chem. Lett.* **2018**, *9* (11), 2733–2738. https://doi.org/10.1021/acs.jpclett.8b00937.
(23) Chen, J.; Yu, T.; Ubba, E.; Xie, Z.; Yang, Z.; Zhang, Y.; Liu, S.; Xu, J.; Aldred, M. P.; Chi, Z. Achieving Dual-Emissive and Time-Dependent Evolutive Organic Afterglow by Bridging Molecules with Weak Intermolecular Hydrogen Bonding. *Adv. Opt. Mater.* **2019**, *7* (7), 1801593. https://doi.org/10.1002/adom.201801593.
(24) Zieger, S. E.; Steinegger, A.; Klimant, I.; Borisov, S. M. TADF-Emitting Zn(II)-Benzoporphyrin: An Indicator for Simultaneous Sensing of Oxygen and Temperature. *ACS Sens.* **2020**, *5* (4), 1020–1027. https://doi.org/10.1021/acssensors.9b02512.
(25) Bhatia, H.; Bhattacharjee, I.; Ray, D. Biluminescence via Fluorescence and Persistent Phosphorescence in Amorphous Organic Donor(D_4)–Acceptor(A) Conjugates and Application in Data Security Protection. *J. Phys. Chem. Lett.* **2018**, *9* (14), 3808–3813. https://doi.org/10.1021/acs.jpclett.8b01551.
(26) Singh, A. K.; Singh, S.; Gupta, B. K. Highly Efficient, Chemically Stable, and UV/Blue-Light-Excitable Biluminescent Security Ink to Combat Counterfeiting. *ACS Appl. Mater. Interfaces* **2018**, *10* (51), 44570–44575. https://doi.org/10.1021/acsami.8b18997.
(27) Hall, D.; Stavrou, K.; Duda, E.; Danos, A.; Bagnich, S.; Warriner, S.; Slawin, A. M. Z.; Beljonne, D.; Köhler, A.; Monkman, A.; Olivier, Y.; Zysman-Colman, E. Diindolocarbazole – Achieving Multiresonant Thermally Activated Delayed Fluorescence without the Need for Acceptor Units. *Mater. Horiz.* **2022**, *9* (3), 1068–1080. https://doi.org/10.1039/D1MH01383A.
(28) Kader, T.; Stöger, B.; Fröhlich, J.; Kautny, P. Azaindolo[3,2,1-Jk]Carbazoles: New Building Blocks for Functional Organic Materials. *Chem. - Eur. J.* **2019**, *25* (17), 4412–4425. https://doi.org/10.1002/chem.201805578.
(29) Hall, D.; Sancho-García, J. C.; Pershin, A.; Ricci, G.; Beljonne, D.; Zysman-Colman, E.; Olivier, Y. Modeling of Multiresonant Thermally Activated Delayed Fluorescence Emitters─Properly Accounting for Electron Correlation Is Key! *J. Chem. Theory Comput.* **2022**, *18* (8), 4903–4918. https://doi.org/10.1021/acs.jctc.2c00141.
(30) Schirmer, J. Beyond the Random-Phase Approximation: A New Approximation Scheme for the Polarization Propagator. *Phys. Rev. A* **1982**, *26* (5), 2395–2416. https://doi.org/10.1103/PhysRevA.26.2395.
(31) Trofimov, A. B.; Schirmer, J. An Efficient Polarization Propagator Approach to Valence Electron Excitation Spectra. *J. Phys. B At. Mol. Opt. Phys.* **1995**, *28* (12), 2299–2324. https://doi.org/10.1088/0953-4075/28/12/003.

(32) Dreuw, A.; Wormit, M. The Algebraic Diagrammatic Construction Scheme for the Polarization Propagator for the Calculation of Excited States. *WIREs Comput. Mol. Sci.* **2015**, *5* (1), 82–95. https://doi.org/10.1002/wcms.1206.
(33) Pershin, A.; Hall, D.; Lemaur, V.; Sancho-Garcia, J. C.; Muccioli, L.; Zysman-Colman, E.; Beljonne, D.; Olivier, Y. Highly Emissive Excitons with Reduced Exchange Energy in Thermally Activated Delayed Fluorescent Molecules. *Nat. Commun.* **2019**, *10* (1), 3–7. https://doi.org/10.1038/s41467-019-08495-5.
(34) Oelkrug, D.; Egelhaaf, H. J.; Haiber, J. Electronic Spectra of Self-Organized Oligothiophene Films with "Standing" and "Lying" Molecular Units. *Thin Solid Films* **1996**, *284–285*, 267–270. https://doi.org/10.1016/S0040-6090(95)08320-0.
(35) Hättig, C.; Hellweg, A.; Köhn, A. Distributed Memory Parallel Implementation of Energies and Gradients for Second-Order Møller-Plesset Perturbation Theory with the Resolution-of-the-Identity Approximation. *Phys. Chem. Chem. Phys.* **2006**, *8* (10), 1159–1169. https://doi.org/10.1039/b515355g.
(36) Grimme, S. Improved Second-Order Møller-Plesset Perturbation Theory by Separate Scaling of Parallel- and Antiparallel-Spin Pair Correlation Energies. *J. Chem. Phys.* **2003**, *118* (20), 9095–9102. https://doi.org/10.1063/1.1569242.
(37) Dunning, T. H. Gaussian Basis Sets for Use in Correlated Molecular Calculations. I. The Atoms Boron through Neon and Hydrogen. *J. Chem. Phys.* **1989**, *90* (2), 1007–1023. https://doi.org/10.1063/1.456153.
(38) Kendall, R. A.; Dunning, T. H.; Harrison, R. J. Electron Affinities of the First-Row Atoms Revisited. Systematic Basis Sets and Wave Functions. *J. Chem. Phys.* **1992**, *96* (9), 6796–6806. https://doi.org/10.1063/1.462569.
(39) Woon, D. E.; Dunning, T. H. Gaussian Basis Sets for Use in Correlated Molecular Calculations. III. The Atoms Aluminum through Argon. *J. Chem. Phys.* **1993**, *98* (2), 1358–1371. https://doi.org/10.1063/1.464303.
(40) Penfold, T. J.; Gindensperger, E.; Daniel, C.; Marian, C. M. Spin-Vibronic Mechanism for Intersystem Crossing. *Chem. Rev.* **2018**, *118* (15), 6975–7025. https://doi.org/10.1021/acs.chemrev.7b00617.
(41) Etherington, M. K.; Gibson, J.; Higginbotham, H. F.; Penfold, T. J.; Monkman, A. P. Revealing the Spin-Vibronic Coupling Mechanism of Thermally Activated Delayed Fluorescence. *Nat. Commun.* **2016**, *7*, 1–7. https://doi.org/10.1038/ncomms13680.

TOC Graphic